NeuroImage 215 (2020) 116822

Contents lists available at ScienceDirect

NeuroImage

journal homepage: www.elsevier.com/locate/neuroimage

Triple visual hemifield maps in a case of optic chiasm hypoplasia

Khazar Ahmadi [a,b], Alessio Fracasso [c,d,e,f,1], Robert J. Puzniak [a,1], Andre D. Gouws [g], Renat Yakupov [h,i], Oliver Speck [h,i,j,k], Joern Kaufmann [l], Franco Pestilli [m], Serge O. Dumoulin [c,e,n], Antony B. Morland [g,o], Michael B. Hoffmann [a,k,*]

[a] Department of Ophthalmology, Otto-von-Guericke University, Magdeburg, 39120, Germany
[b] Clinical Memory Research Unit, Department of Clinical Sciences, Lund University, Lund, 22362, Sweden
[c] Department of Experimental Psychology, Helmholtz Institute, Utrecht University, Utrecht, 3584 CS, the Netherlands
[d] Department of Radiology, University Medical Center Utrecht, Utrecht, 3584 CX, the Netherlands
[e] Spinoza Centre for Neuroimaging, Amsterdam, 1105 BK, the Netherlands
[f] Institute of Neuroscience and Psychology, University of Glasgow, Glasgow, G12 8QB, UK
[g] Department of Psychology, York Neuroimaging Centre, University of York, York, YO10 5NY, UK
[h] Department of Biomedical Magnetic Resonance, Institute for Physics, Otto-von-Guericke University, Magdeburg, 39120, Germany
[i] German Center for Neurodegenerative Diseases, Magdeburg, 39120, Germany
[j] Leibniz Institute for Neurobiology, Magdeburg, 39118, Germany
[k] Center for Behavioral Brain Sciences, Magdeburg, 39106, Germany
[l] Department of Neurology, Otto-von-Guericke-University, Magdeburg, 39120, Germany
[m] Department of Psychological and Brain Sciences, Indiana University, Bloomington, IN, 1101 E, USA
[n] Department of Experimental and Applied Psychology, VU University Amsterdam, Amsterdam, 1081 BT, the Netherlands
[o] Centre for Neuroscience, Hull-York Medical School, University of York, York, YO10 5DD, UK

ARTICLE INFO

Keywords:
DWI
fMRI
Optic chiasm
Plasticity
Retinotopy
Visual cortex

ABSTRACT

In humans, each hemisphere comprises an overlay of two visuotopic maps of the contralateral visual field, one from each eye. Is the capacity of the visual cortex limited to these two maps or are plastic mechanisms available to host more maps? We determined the cortical organization of the visual field maps in a rare individual with chiasma hypoplasia, where visual cortex plasticity is challenged to accommodate three hemifield maps. Using high-resolution fMRI at 7T and diffusion-weighted MRI at 3T, we found three hemiretinal inputs, instead of the normal two, to converge onto the left hemisphere. fMRI-based population receptive field mapping of the left V1–V3 at 3T revealed three superimposed hemifield representations in the left visual cortex, i.e. two representations of opposing visual hemifields from the left eye and one right hemifield representation from the right eye. We conclude that developmental plasticity including the re-wiring of local intra- and cortico-cortical connections is pivotal to support the coexistence and functioning of three hemifield maps within one hemisphere.

1. Introduction

Topographic maps of the contralateral visual field are instrumental for the functionality of the human visual cortex and are considered a core principle of the notion of hemispheric specialization (Huberman et al., 2008; Wandell et al., 2007). A fundamental prerequisite for the formation of these maps is the partial decussation of the optic nerves at the optic chiasm. Here, the fate of axons from the eyes is decided such that axons from the nasal retina cross the midline and project to the contralateral hemisphere, while fibers from the temporal retina remain uncrossed and project ipsilaterally. As a consequence of this partial decussation, each hemisphere receives binocular input from the contralateral visual field. While acquired damage to the optic chiasm results in bitemporal hemianopia (Weber and Landau, 2013), congenital chiasma malformations leave major aspects of visual function intact (Hoffmann et al., 2007; Hoffmann and Dumoulin, 2015; Klemen et al., 2012). This renders these conditions invaluable models to study the foundations of visual pathway formation and the scope of its plasticity in humans.

In individuals affected with congenital chiasmatic abnormalities [absence of optic nerve crossing in achiasma and hemihydranencephaly

* Corresponding author. Department of Ophthalmology, Otto-von-Guericke University, Leipziger Str. 44, 39120, Magdeburg, Germany.
E-mail address: michael.hoffmann@med.ovgu.de (M.B. Hoffmann).
[1] These authors contributed equally.

https://doi.org/10.1016/j.neuroimage.2020.116822
Received 30 August 2019; Received in revised form 27 February 2020; Accepted 2 April 2020
Available online 8 April 2020

(Apkarian et al., 1994; Fracasso et al., 2016; Hoffmann et al., 2012; Muckli et al., 2009; Victor et al., 2000) or enhanced crossing in FHONDA and albinism (Ahmadi et al., 2019; Apkarian et al., 1983; Hoffmann et al., 2003; von dem Hagen et al., 2008)], the visual cortex receives erroneous input from the ipsilateral visual field in addition to the normal input from the contralateral visual field. This results, at the macroscopic scale, in two superimposed retinotopic maps of opposing hemifields in V1 (Ahmadi et al., 2019; Bao et al., 2015; Davies-Thompson et al., 2013; Hoffmann et al., 2012, 2003; Kaule et al., 2014; Muckli et al., 2009). Remarkably, at the mesoscopic scale, these maps are interdigitated and form hemifield dominance domains (Olman et al., 2016), that are reminiscent of the ocular dominance domains in the normal visual system. It appears therefore that the reassignment of ocular dominance domains to hemifield dominance domains is a simple mechanism to accommodate two hemifield maps, either two representations of one visual hemifield via binocular input in normal vision or two representations of opposing hemifields via monocular input in congenital chiasma malformations (Hoffmann and Dumoulin, 2015).

These observations prompt the important question, whether V1 is limited to hosting two hemifield maps, or whether the scope of plasticity in human V1 allows for the accommodation of even more maps. To address this question, we determined the cortical organization in an individual with chiasma hypoplasia whose misrouting pattern deviated from the typical hallmark of complete achiasma, i.e., the entire absence of crossing projections. In fact, the clinical spectrum of congenital achiasma ranges between the complete absence of the optic chiasm and consequently an absence of crossing nasal fibers i.e., complete achiasma, to a hypoplastic optic chiasm with a reduction of crossing nasal fibers (Sami et al., 2005). This is depicted as a schematic in Fig. 1, which juxtaposes control, complete achiasma, and the case of chiasma hypoplasia investigated in the present study.

The mechanism of reassigning ocular dominance domains alone would suggest that only two inputs can be accommodated, so any additional input would necessarily need to engage further plastic mechanisms to establish a useful visual representation. The condition of chiasma hypoplasia provides the opportunity to explore the limits of plasticity in V1 and beyond.

Three types of investigations were performed using 3 and 7 T MRI: (i) diffusion-weighted imaging (DWI) to specify the projection error of the optic nerves at the optic chiasm, (ii) population receptive field (pRF) mapping (Ahmadi et al., 2019; Dumoulin and Wandell, 2008) to determine the cortical visual field maps, and (iii) high-resolution fMRI. Our results demonstrate that maps from three hemifields can be accommodated within a single V1. We propose that mechanisms of developmental plasticity that are exceeding the simple reassignment of ocular dominance domains to hemifield dominance domains enable these three maps to be hosted in V1.

2. Materials and methods

2.1. Case description

A 26-year-old female with **c**hiasma **hypo**plasia ('CHP') participated in the study. Her best-corrected decimal visual acuity (Snellen acuity) was 0.63 (20/32) for the dominant right eye and 0.25 (20/80) for the left eye. She had moderate vertical nystagmus, strabismus [alternating strabismus, esotropia (5°), and vertical deviation (7°) with alternating suppression of each eye] and no stereoscopic vision. Humphrey-like visual field testing revealed normal visual fields in both eyes. Decussation anomalies were confirmed with visual evoked potentials (VEPs) and T1-weighted MRI at the age of 22. She reported an otherwise normal developmental and medical history and there was no family history of ophthalmological or neurological disorders. MRI measurements on CHP were performed at two sites. CHP was first scanned at Magdeburg University, Germany, at the age of 24. In two consecutive days, she underwent high-resolution fMRI at 7T and DWI scanning sessions at 3T. Due to limited availability of CHP, pRF mapping data were acquired two years later at York Neuroimaging Center, UK, at 3T.

2.2. Control Participants

12 respective control participants were also included in the current study. The first four controls (C1 – C4; mean age = 31, range = 25–49 years, 2 females) took part in a pRF mapping session at 3T while the other eight controls (C5 – C12, mean age = 29, range = 22–52 years, 6 females) participated in the DWI sessions. The last control participant (C12) also underwent high-resolution fMRI at 7T. All experiments on controls were conducted in Magdeburg. Informed written consent was obtained from all participants prior to the study investigations. The procedures followed the tenets of the declaration of Helsinki and the respective protocols were approved by the ethical committees of the University of Magdeburg and York Neuroimaging Centre.

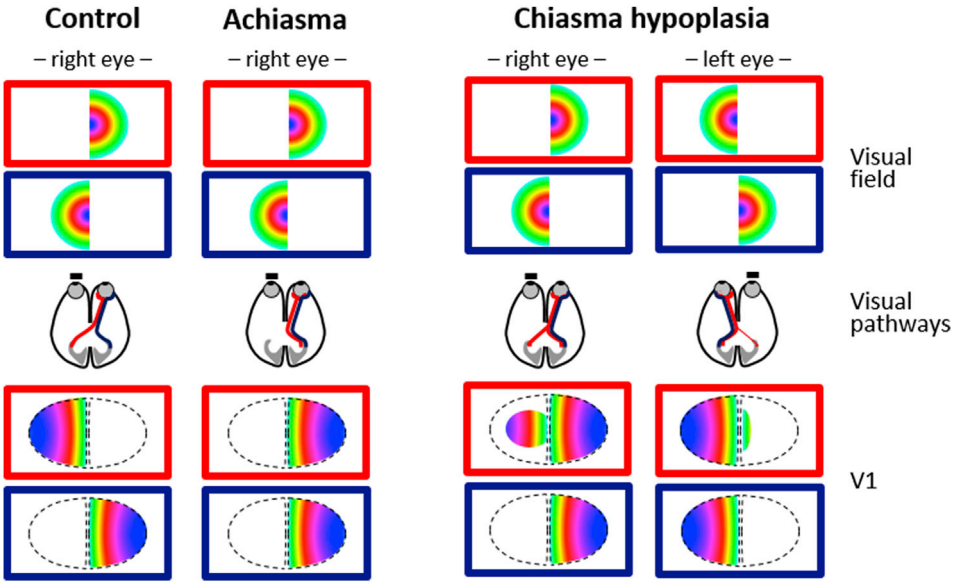

Fig. 1. Schematic optic nerve projections and eccentricity representations in V1 for control, achiasma, and chiasma hypoplasia. Control (right eye): the nasal (red) and temporal (blue) retinal fibers of the right eye project to the left and right hemispheres respectively (frame color follows fiber color coding). Consequently, the eccentricity representations reside in the V1 contralateral to the respective hemifield. **Achiasma (right eye):** Due to the complete absence of crossing nasal fibers, the right V1 is organized as a cortical overlay of orderly eccentricity maps from both the contra- and ipsilateral hemifields. **Chiasma hypoplasia (right and left eyes):** Similar to complete achiasma, the predominance of non-crossing nasal fibers leads to the superimposed eccentricity maps of opposing hemifields in V1. In contrast to complete achiasma, however, there is a portion of crossing nasal fibers resulting in a residual representation of the contralateral hemifield via the contralateral eye in V1. As a consequence, each hemisphere receives not only input from the ipsilateral, but also some input from the contralateral eye.

2.3. High-resolution fMRI

Visual stimulation: Visual stimuli were presented by back-projection onto a screen with a resolution of 1920 X 1080 pixels and viewed at a distance of 100 cm via an angled mirror. Presentation software package (Neurobehavioral Systems, Berkeley, CA, USA) was used to control stimulus presentation. The stimuli extended ±12.9° by ± 7.4° of visual angle from the center of the screen and comprised bilateral, contrast reversing (8 reversals per second) black and white checkerboards with 24 segments and 26 rings (mean luminance 62 cd/m^2, contrast 99%). A block design, alternating between the two eyes was selected. It consisted of 14 checkerboard presentation blocks (7 blocks per eye), each of which lasted for 12 s and was followed by a rest block (mean luminance gray background) with the same duration. The presentation blocks were preceded by an additional rest block of 12 s for dummy stimulation. Participants wore a custom-made manually operated shutter that allowed monocular viewing through either the left or right eye. They fixated a central fixation cross, which changed its color 1 s after initiation of each rest block, lasting for 23 s (11 s of the rest block plus 12 s of the next presentation block). The participants were requested to occlude the right eye and view the stimuli with the left eye for a green fixation cross, and vice versa for a red one. An MRI-compatible camera was used to view the dominant eye, to ensure that the participants were doing the task correctly.

MRI acquisition: For functional imaging, T2*-weighted volumes were acquired using a 2D gradient-echo EPI sequence with a 7T whole body MRI scanner (Siemens Healthineers, Erlangen, Germany) using a 32 channel head coil (Nova Medical, Wilmington, MA) with the following acquisition parameters: TR | TE = 3000 | 22 ms, flip angle = 90°, FOV = 169 (right-left) × 130 (anterior-posterior) × 27 (feet-head) mm^3, acceleration factor (r) = 4 with GRAPPA reconstruction, phase-encoding direction = right-left, phase partial Fourier = 5/8, bandwidth (BW) = 1086 Hz/px, echo-spacing = 1.13 ms and voxel size = 0.65 x 0.65 × 0.65 mm^3. Forty-one oblique axial slices were acquired for the duration of 348 s with 116 time frames, of which the first four were discarded. The slice placement for the functional volumes covered a portion of the occipital cortex parallel to the calcarine sulcus. Foam padding was used to minimize head motion. Four runs of bilateral stimulation were performed for each participant in a single session.

A high-resolution anatomical volume was obtained using a 3D T1-weighted MPRAGE sequence (TR | TE | TI = 2500 | 2.76 | 1050 ms, total duration = 14:14 min, flip angle = 5°, FOV: 350 × 263 × 350 mm^3, and voxel size = 0.65 × 0.65 × 0.65 mm^3). In addition, a proton density weighted volume without the inversion module (identical parameters except for TR = 1820 ms and total duration = 5:33 min) was acquired to correct for receive coil biases (Van de Moortele et al., 2009).

Data analysis: To obtain an inhomogeneity corrected anatomical volume, the T1-weighted MPRAGE reference volume was divided by the proton density weighted volume. Gray and white matter (GM/WM) were segmented based on the resulting anatomical volume in MIPAV (https://mipav.cit.nih.gov/) using the TOADS/CRUISE algorithm (Bazin and Pham, 2007; Han et al., 2004). Manual editing was performed in ITK-GRAY (https://web.stanford.edu/group/vista/cgi-bin/wiki/index.php/ItkGray) to minimize the segmentation error. An equi-volume distance map was employed (Waehnert et al., 2014) to build a coordinate system along the cortical depth, taking the local curvature into account.

The functional data were corrected for motion artifacts and spatial distortion using MCFLIRT function of FSL (https://www.fmrib.ox.ac.uk/fsl) and a point spread function (PSF) mapping method (In and Speck, 2012) respectively. Motion and distortion corrected data were then analyzed using AFNI (https://afni.nimh.nih.gov/afni). Time series were averaged across repetitions for each participant to increase the signal-to-noise ratio (SNR). Afterwards, the averaged functional volume was aligned to the T1-weighted anatomical volume using an affine transformation. The alignment was performed in three steps: First, the T1-weighted anatomy and the averaged EPI were clipped in the anterior-posterior direction, leaving only the occipito-temporal cortex. A good starting point was provided by centering the functional volume on the anatomy using the respective centers of mass. Next, the averaged functional volume was affinely aligned to the T1-weighted volume via AFNI's 'align_epi_anat.py' with the local Pearson's coefficient (LPC) cost function (Saad et al., 2009), using the two-pass option. This procedure blurs the functional volume and initially allows for large rotation and shift, and then refines the alignment by an affine transformation. Finally, the resulting alignment was further improved via 3dAllineate, using the one-pass option. In this step, the functional volume is not blurred. Only a small amount of shift and rotation is allowed, using an affine transformation that is obtained by concatenating the transformation matrices generated in previous steps (Fracasso et al., 2018; Klein et al., 2018).

A general linear model (GLM) was used to analyze the functional data. For each voxel, the percentage of BOLD signal changes to stimulation of the left and right eye was estimated via 3dDeconvolve function of AFNI. Nuisance regressors were modelled using polynomials up to the second order to remove any linear and quadratic trends. The GLM analysis was performed on the native EPI space. The obtained GLM maps (F-maps and beta-coefficient-maps) were co-registered to the T1-weighted space using the affine transformation matrix estimated in the alignment step. Multiple comparisons were corrected using false discovery rate (FDR) with a q value of 0.045. For each of the cortical layers, a 3D mesh was generated using AFNI's IsoSurface function.

2.4. Diffusion-weighted imaging

MRI acquisition: DWI data were acquired using a 3T MAGNETOM Prisma syngo MR D13D scanner (Siemens Healthineers, Erlangen, Germany) with a 64 channel head coil. MRI acquisition was initiated by a localizer scan, followed by a T1-weighted and two diffusion-weighted scans. All data were collected during a single scanning session. The T1-weighted volume was obtained in sagittal orientation using a 3D-MPRAGE sequence (TE | TR = 4.46 | 2600 ms, TI = 1100 ms, flip angle = 7°, resolution = 0.9 x 0.9 × 0.9 mm^3, FoV = 230 × 230 mm^2, image matrix = 256 × 256 x 176, acquisition time (TA) = 11:06 min). The first diffusion-weighted scan was acquired with Echo-Planar Imaging (EPI) with the following parameters: b-value = 1600 s/mm^2, TR | TE = 9400 | 64.0 ms, voxel size = 1.5 x 1.5 × 1.5 mm^3, phase-encoding direction = anterior to posterior, FoV = 220 × 220 mm^2, and TA = 22:24 min. Scanning was performed with 128 unique gradient directions, thus the obtained diffusion-weighted data can be described as High Angular Resolution Diffusion Imaging (HARDI) data (Tuch et al., 2002). Gradient tables were generated using E. Caruyer's tool for q-space sampling (Caruyer et al., 2013). Diffusion-weighted volumes were evenly intersected by 10 non-diffusion weighted volumes for the purpose of motion correction. The second diffusion-weighted scan was acquired with identical parameters except for reversed phase-encoding direction in comparison to the preceding scan, i.e., posterior to anterior direction. Acquisition of two diffusion-weighted scans with opposite phase-encoding directions enhances the correction of susceptibility-induced geometric distortion (Andersson et al., 2003) and improves the SNR of the total DWI data.

Data analysis: Conversion of DICOM images to NIFTI format, denoising of the DWI data and removal of Gibbs ringing were performed with MRtrix 3.0 (http://www.mrtrix.org/). FSL was employed for the correction of susceptibility-induced geometric distortions, eddy current distortions, and motion artifacts. The bias field in the DWI data was corrected using ANTS (http://stnava.github.io/ANTs/). Afterwards, DWI data were co-registered to the T1-weighted volume, which was aligned beforehand to Anterior Commissure – Posterior Commissure line, via mrDiffusion (https://github.com/vistalab/vistasoft/tree/master/mrDiffusion). The T1-weighted volume was automatically segmented using FIRST function of FSL. Subsequently, manual editing was performed to mitigate segmentation errors in the region of the optic chiasm.

Each voxel of the preprocessed DWI data was modelled using the Constrained Spherical Deconvolution (CSD) approach (Tournier et al.,

2008), which is particularly sensitive when resolving populations of crossing fibers, like those observed in the optic chiasm, and benefits from the high angular resolution of HARDI data. The application of the CSD model involved the estimation of single fiber response function with Tournier's algorithm (Tournier et al., 2013) for maximum harmonic order (Lmax = 6) and the estimation of fiber orientation distribution functions (Jeurissen et al., 2014) for 3 different maximum harmonic orders i.e. Lmax = 6, 8 and 10. Four ROIs were manually drawn on the T1-weighted volume, two covering cross-sections of the two optic nerves, and the other two covering cross-sections of the two optic tracts. The ROIs were placed as close to the optic chiasm as possible, but did not intersect it. Each ROI had a width of 3 voxels (anterior-posterior) to assure proper streamline termination during tractography. Fiber tracking was performed between the ROIs of the two optic nerves as seeds and the ROIs of the two optic tracts as targets, resulting in 4 connectivity pairs (2 ipsilateral and 2 contralateral fiber bundles). Tracking was done in two directions i.e. from seed to target ROI and backwards to ensure the indifference of the results to direction of tracking. The corresponding generated connectivity pairs were subsequently merged together. The tracking employed an ensemble tractography (ET) framework (Takemura et al., 2016), where tracking is performed several times, each time for a different set of parameters. As such, the bias in the outcome tracts, caused by parameter selection, is avoided. The tracking was performed with the probabilistic tracking algorithm iFOD2 (Tournier et al., 2010) using unique combinations of 2 different fractional anisotropy (FA) thresholds (FA = 0.04 and 0.08), 3 maximum curvature angles (30°, 45°, 60°), and 3 CSD models estimated for different maximum harmonic orders (L_{max} = 6, 8, 10) for each of 139,000 seeding attempts. Additionally, tractography employed an anatomically-constrained tractography (ACT) approach (Smith et al., 2012), which constrains tractography with anatomical priors derived from the anatomical image using white/gray matter, subcortical gray matter and CSF masks obtained with FSL's FIRST function. As a result of the tractography, 4 streamline groups corresponding to 4 distinct connectivity pairs were obtained. The proportion of streamlines in each group was subsequently used as an estimate of the connectivity strength in the optic chiasm.

2.5. Population receptive field (pRF) and connective field (CF) modeling

Visual stimulation: Visual stimuli consisted of drifting bar apertures (stimulus size in York and Magdeburg: 11° and 10° radius, respectively), exposing a moving high-contrast checkerboard pattern (Dumoulin and Wandell, 2008) at four different directions i.e. upward, downward, left and right. The bars were presented to each eye separately within a mask, covering either the left or the right hemifields for stimulation of either the nasal or the temporal retina in separate experiments. The width of the bars subtended one-quarter of the stimulus radius. Each pass of the bars lasted for 30 s, followed by a mean luminance block (zero contrast) of 30 s. The stimuli were generated in MATLAB (Mathworks, Natick, MA, USA) using the Psychtoolbox (Brainard, 1997; Pelli, 1997) and rear-projected onto a screen (screen resolution in York and Magdeburg: 1920 x 1080 and 1140 x 780 pixels, respectively) inside the magnet bore. In York, CHP viewed the screen at a distance of 57 cm via an angled, front-silvered mirror whereas the eye to screen distance in Magdeburg was 35 cm. Participants were required to fixate a centered dot and to report color changes between red and green by means of a button press.

MRI acquisition: Identical 3T Prisma scanners (Siemens Healthineers, Erlangen, Germany) were used at both sites. At York Neuroimaging Center, functional T2*-weighted volumes were acquired with a 64 channel head coil. A total of 30 EPI slices were obtained within a FOV of 192 mm, with 3 x 3 × 3 mm^3 voxels (TR | TE = 1500 | 26 ms and flip angle = 80°). Each functional scan comprised 168 time frames, lasting for 252 s. The first eight time-frames (12 s) were removed to allow magnetization to reach a steady-state. Foam padding was used to minimize head motion. Additionally, a T1-weighted anatomical volume was acquired at a resolution of 1 x 1 × 1 mm^3 (TR | TE = 2500 | 42.26 ms and flip angle = 7°). Eight functional scans were obtained in a single session (4 scans per eye). The right eye was stimulated during the first 4 runs while the left eye was patched. The stimulation of each of the left and right hemifields was repeated twice in a counterbalanced manner. After a short break in the scanning, the left eye was stimulated while the right eye was occluded. The same stimulation procedure was performed for the left eye. At Magdeburg University, functional images (TR | TE = 1500 | 30 ms and flip angle = 70°) were acquired at a resolution of 2.5 x 2.5 × 2.5 mm^3 with 54 axial slices, using a 64 channel head coil. Every functional scan had 168 time frames (252 s). In addition, a high resolution whole-brain anatomical volume (voxel size = 0.9 x 0.9 × 0.9 mm^3, TR | TE = 2600 | 4.46 ms, and flip angle = 7°) was obtained. Foam padding limited the head movements. In each session, left and right hemifield stimulation conditions were performed monocularly and repeated six times (three repetitions per hemifield).

Data analysis: The same analysis pipeline was used for data sets acquired in both sites. The T1-weighted anatomical volume was automatically segmented using the recon-all function of FreeSurfer (https://surfer.nmr.mgh.harvard.edu). The cortical surface was reconstructed at the white/gray matter boundary and rendered as a smoothed 3D mesh (Wandell et al., 2000). The MCFLIRT function of FSL was used for motion correction of the functional data. Motion corrected data were then analyzed using freely available Vistasoft software package for MATLAB (https://github.com/vistalab/vistasoft). Time series for the same conditions were averaged together for each participant to increase the SNR. Afterwards, the averaged functional image was co-registered to the anatomical scan using a combination of Vistasoft and Kendrick Kay's alignment tools (https://github.com/kendrickkay/alignvolumedata). Visual areas were mapped using the population receptive field (pRF) modeling (Dumoulin and Wandell, 2008). Briefly, the BOLD (blood oxygen level dependent) response of each voxel was predicted using a 2D-Gaussian model of the neuronal populations defined by three stimulus-referred parameters i.e. x0, y0, σ where x0 and y0 are the coordinates of the receptive field center and σ is it's spread (Dumoulin and Wandell, 2008; Fracasso et al., 2016; Harvey and Dumoulin, 2011). The predicted BOLD signal was then calculated by convolution of the stimulus sequence for the respective pRF-model and its three parameters with the canonical hemodynamic response function (Friston et al., 1998). The optimal pRF parameters were found by minimizing the sum of squared errors (RSS) between the predicted and observed BOLD time-course. For all subsequent analyses including derivation of the polar angle and eccentricity maps, required for the delineation of the visual areas, and the visualization on the inflated cortical surface, only the voxels were included whose pRF fits exceeded 15% of the variance explained.

The connective field parameters were estimated from the fMRI time-series, using CF modeling method that predicts the neuronal activity in one brain area with reference to aggregate activity in another area (Haak et al., 2013). The BOLD response in each voxel of a target ROI i.e. V2 or V3, was predicted with a symmetrical, circular 2D Gaussian CF model folded to follow the cortical surface of the source ROI, i.e. V1. The CF model was defined by two parameters i.e. Gaussian position and spread across the cortical surface. The optimal CF parameters were determined by minimizing the residual sum of squares between the predicted, and the observed time-series. For this purpose, many fMRI time-series predictions were generated by changing the CF positions across all voxel positions and Gaussian spread values on the surface of the source ROI. Best models were selected when the explained variance in the fMRI time-series survived a threshold of 15%.

2.6. 2.6 Visual field testing

We simulated the Humphrey visual field testing using PsychoPy (https://www.psychopy.org) on a calibrated CRT monitor (22-inch Mitsubishi, 2070SB at 85 Hz). Background luminance was set to 10 cd/m^2, equal to 30 dB. Goldmann size III stimuli i.e., white circular patches (0.43° diameter) were displayed for 235 ms and placed at 54 locations

according to the Humphrey 24-2 standard test. In addition, four stimuli were placed at 12, 15, 18, and 21° into the temporal field along the horizontal meridian in order to capture the blind spot. The detection threshold was tested in both eyes with one-up-one down staircase procedure with a minimum of 30 trials per location. Responses were within 800 ms after the stimulus presentation. An initial adaptive staircase with 4 dB/2 dB step sizes was used to coarsely estimate the threshold at 16 locations in the visual field (4 in each visual quadrant), starting at the maximum gun value. Subsequently, a second adaptive staircase with finer step sizes (minimum 0.25 dB) was used to more accurately find the threshold starting at a gun value of 25% of the maximum (35 cd/m^2).

3. Results

3.1. Atypical lateralization pattern revealed by high-resolution fMRI data

High-resolution fMRI at 7T was used to evaluate the cortical lateralization pattern in response to bilateral contrast reversing black and white checkerboards presented to each eye separately (see Methods). In a neuro-typical visual system, bilateral stimulation of each eye leads to bihemispheric activation (Figure S1). In CHP, however, bilateral stimulation of the left eye yielded predominant responses on the ipsilateral occipital cortex i.e. on the left hemisphere, and only a marginal activation was observed on the contralateral hemisphere (Fig. 2A). In contrast, considerable bilateral activation was found during bilateral stimulation of the right eye (Fig. 2B). It should be noted that regardless of the stimulated eye, the contralateral activity in CHP was weaker compared to the control participant (the ratio of contralaterally activated voxels to all active i.e. ipsilateral plus contralateral voxels for left and right eye stimulation, respectively in CHP: 5.4% and 20.1%, and in control: 51.3% and 50.6%). Nonetheless, the robust activation on the left hemisphere upon the stimulation of the right eye in CHP indicated that part of the nasal afferents decussate at the chiasm and project to the contralateral hemisphere. This revealed that her misrouting pattern is distinct from complete achiasma where bilateral stimulation of each eye results in complete ipsilateral activation.

3.2. Optic nerve misrouting revealed with DWI

The above results predicted that the proportion of crossing fibers from the right eye would exceed that from the left eye. More direct evidence for this specific misrouting of the optic nerves in CHP was provided by a quantitative assessment of the streamlines at the optic chiasm based on DWI data (see Methods). For CHP and 8 individuals of a control cohort, a total of four ROIs were selected, one in each of the two optic nerves and one in each of the two optic tracts, to identify streamlines connecting each optic nerve with the (i) ipsilateral and (ii) contralateral optic tract, i.e. uncrossed and crossed projections.

The results are presented in Table 1. The proportion of the uncrossed, i.e. ipsilateral, projections was similar for the right and left optic nerves in CHP and within the ranges observed in controls though not between the first and third quartiles. In contrast, the proportion of the crossed, i.e. contralateral, projections was far greater for the right than for the left eye in CHP, exceeding the observed range for the right eye in controls (see Table 1). This underscores the asymmetric distribution of crossing

Table 1
Comparison of ipsi- and contralateral streamlines between right and left eye of CHP and controls. It should be noted, that the values indicate the proportion of ipsilateral streamlines of each eye relative to all ipsilateral streamlines, and the proportion of contralateral streamlines of each eye relative to all contralateral streamlines; i.e., the values are not the proportion of ipsilateral or contralateral projections relative to all streamlines.

		Ipsilateral streamlines per eye normalized to all ipsilateral streamlines		Contralateral streamlines per eye normalized to all contralateral streamlines	
		right eye	left eye	right eye	left eye
CHP	Value	42%	58%	73%	27%
Controls	Values range	40–68%	32–60%	39–68%	32–61%
	Median	54%	46%	48%	52%
	1st and 3rd quartile	47 and 58%	43 and 53%	42 and 59%	41 and 58%

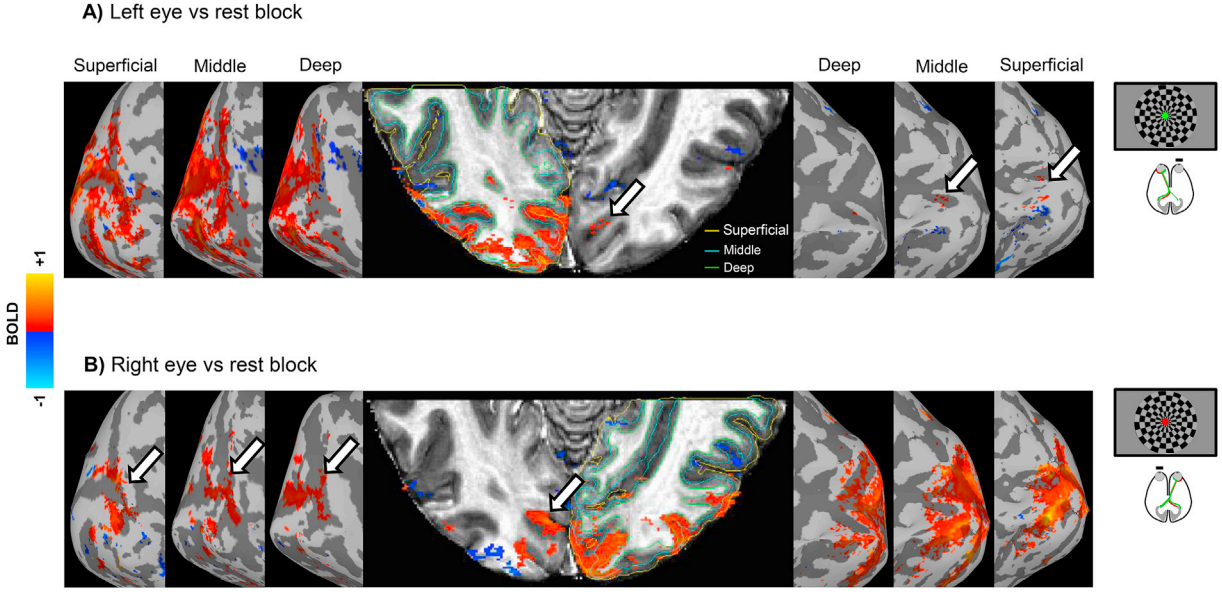

Fig. 2. Cortical response lateralization during bilateral stimulation of each eye in CHP. The cortical activation is projected onto a clipped anatomical image of the occipital cortex and onto the inflated cortical surfaces of the deep, middle, and superficial layers. **A)** Left eye stimulation vs rest elicits predominantly unilateral activation on the ipsilateral hemisphere with a small residual activation on the contralateral hemisphere, indicated by white arrows. **B)** Right eye stimulation vs rest elicits bilateral activation, i.e. on the ipsilateral hemisphere and also on part of the contralateral hemisphere (white arrows). The activation maps consist of signal amplitude expressed as the β coefficient from the GLM thresholded by cluster size and F statistic (cluster = 20, threshold by F = 10.477 and 10.040 for **A** and **B**, respectively, $p < 0.002$, corrected). Note that the cortical surfaces are generated from different cortical depths. Consequently, they look different, delimit to different volumes and have different number of nodes.

afferents at the optic chiasm in CHP, which is in accordance with the above fMRI findings. A 3D rendering of the tracked streamlines is illustrated in Fig. 3.

The proportion of the contra- and ipsilateral streamlines in CHP was further compared to all controls as well as an individual with complete achiasma and a cohort of 9 albinotic participants whose tractography results were extracted from a previous study (Puzniak et al., 2019). As expected, the crossing at the optic chiasm in CHP was lower than the controls and the cohort with albinism and higher than the participant with complete achiasma (see Figure S2).

3.3. Three overlaid hemifield representations revealed by pRF mapping

Based on the response lateralization pattern observed in the high-resolution fMRI data, we speculated that a significant part of the visual cortex on the left occipital lobe receives input from three hemiretinae, from the two hemiretinae of the ipsilateral, i.e. left, eye and from the nasal hemiretina of the contralateral, i.e. right eye. To test this hypothesis and to determine the specific mapping of the three inputs, pRF mapping (Dumoulin and Wandell, 2008) was performed during monocular stimulation of each eye and hemifield separately (see Methods). In the control participant, visuotopic maps of each hemifield were found on the contralateral hemisphere (Fig. 4). Remarkably, stimulation of the left eye in CHP revealed orderly organized eccentricity and polar angle maps of both ipsi- and contralateral hemifields on the left hemisphere across the three early visual areas (V1–V3; Fig. 5 A & B). Left and right hemifield representations were superimposed within each visual area in a mirror-symmetrical manner, in accordance with previous reports of complete achiasma (Hoffmann et al., 2012; Kaule et al., 2014). There was a small normal representation along the horizontal meridian on the contralateral, i.e. right, hemisphere (Fig. 5B).

For hemifield mapping of the right eye in CHP, a similar picture was obtained, i.e. mirror-symmetrical superposition of orderly visuotopic maps of opposing hemifields (Fig. 5 C & D). Importantly, the residual normal representation from the right eye was much more extensive than that from the left eye (Fig. 5C), which is consistent with the above high-resolution fMRI at 7T and DWI findings. The activation patterns measured at 7T (Fig. 2B), specifically in the middle and superficial layers, largely correspond to the residual representation from the right eye observed in Fig. 5C. It should be noted that there is stronger contralateral activity from the right eye for 7T compared to 3T fMRI, likely due to enhanced SNR for the former. This might also be the cause of the emergence of response signature in the dorsal portions of the early visual cortex for the 7T data. Importantly, the residual normal representation on the left hemisphere appeared to be superimposed onto the other two maps from the left eye (Fig. 5 A & B). As shown in Fig. 5C, the residual normal representation of the right hemifield covered a large part of V1 and spanned the entire polar angle range, from the lower vertical meridian in the dorsal portion of V1, through the horizontal and to the upper vertical meridian in the ventral portion of V1 and thus followed the normal retinotopic pattern. The observed retinotopic pattern of this residual input was not restricted to V1 and partially spread to V2 and V3.

In conclusion, we found a superposition of three retinotopic representations i.e., two representations from opposing visual hemifields mediated by the left eye plus an additional representation of the contralateral hemifield from the right eye, in the left hemisphere of CHP. This is in contrast to the retinotopic organization of the neuro-typical visual system where each hemifield is represented on the contralateral hemisphere (Fig. 4). A summary of this finding is provided in Fig. 6 which illustrates the co-localization of three retinotopic representations in the left visual cortex of CHP. Furthermore, the comparison of the eccentricity values between the representations of the i) right vs left hemifields of the left eye, ii) right hemifield of the left vs right hemifield of the right eye, and iii) right hemifield of the right eye vs left hemifield of the left eye revealed a good alignment of the three retinotopic representations within the area of overlap in the left V1 ($R^2 = 0.81$, 0.15, and 0.16 respectively, $p < 0.00001$ for all three comparisons; see Figure S3). The lower R^2 values observed for the two later comparisons might be associated with a slight shift in the eccentricity maps as evident in Fig. 5B and C, which could be attributed to the noise intrusion in the data, possibly due to imperfect fixation. As the circular nature of the polar angle values is a confound of this analysis, it was only performed for the eccentricity values.

3.4. Responsivity of the visual cortex receiving triple hemifield input

The above findings prompted the question of the functional characteristics of these maps in V1 and beyond. To compare the activation of the early visual cortex across the three hemifield-mapping conditions and to assess how the activation is propagated from V1 to V2 and V3, we determined the area of activated cortex in the early areas of the left hemisphere of CHP. As a reference, we used the condition of contralateral hemifield mapping via the left, i.e. ipsilateral, eye (normal input) for normalization and thus determined the relative activated area for both ipsilateral hemifield mapping via the left eye (abnormal input) and contralateral hemifield mapping via the right eye (residual normal input). The normal and abnormal inputs from the left eye activate a similar expanse of V1, V2 and V3. In contrast, the residual normal input from the right eye activates smaller proportions of V1, V3, and specifically V2 (Fig. 7A).

Subsequently, we obtained a measure of the reliability of the input for the ROIs that comprise the overlay of the three hemifield representations

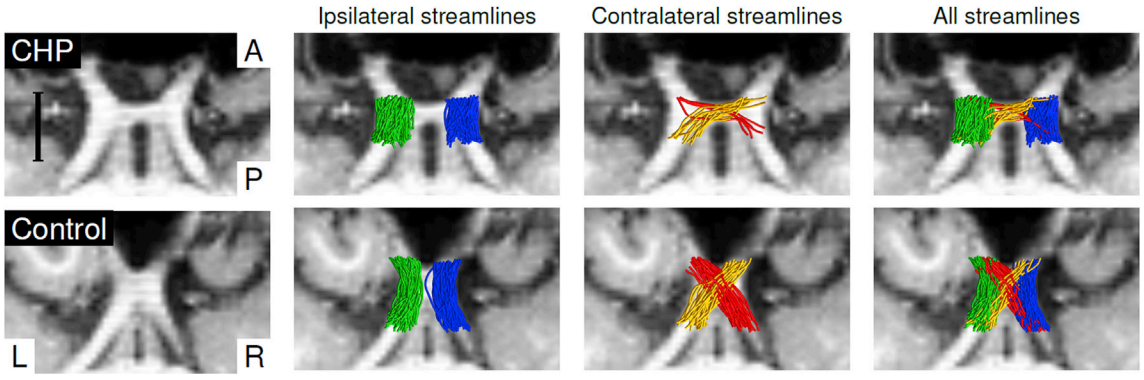

Fig. 3. Tractography of the optic chiasm. Axial slices without and with tractography overlay. The scale bar represents 1 cm. L-R and A-P stand for left-right and anterior-posterior directions, respectively. **Top row)** in CHP, the ipsilaterally projecting streamlines (blue and green for right and left optic nerve, respectively) are largely symmetrically distributed, while there is a predominance of contralaterally projecting streamlines for the right compared to the left optic nerve (yellow and red, respectively). **Bottom row)** in the control participant, both ipsi- and contralaterally projecting streamlines of the right and left optic nerves are largely symmetrically distributed. For clarity, only 0.25% of the generated streamlines are rendered.

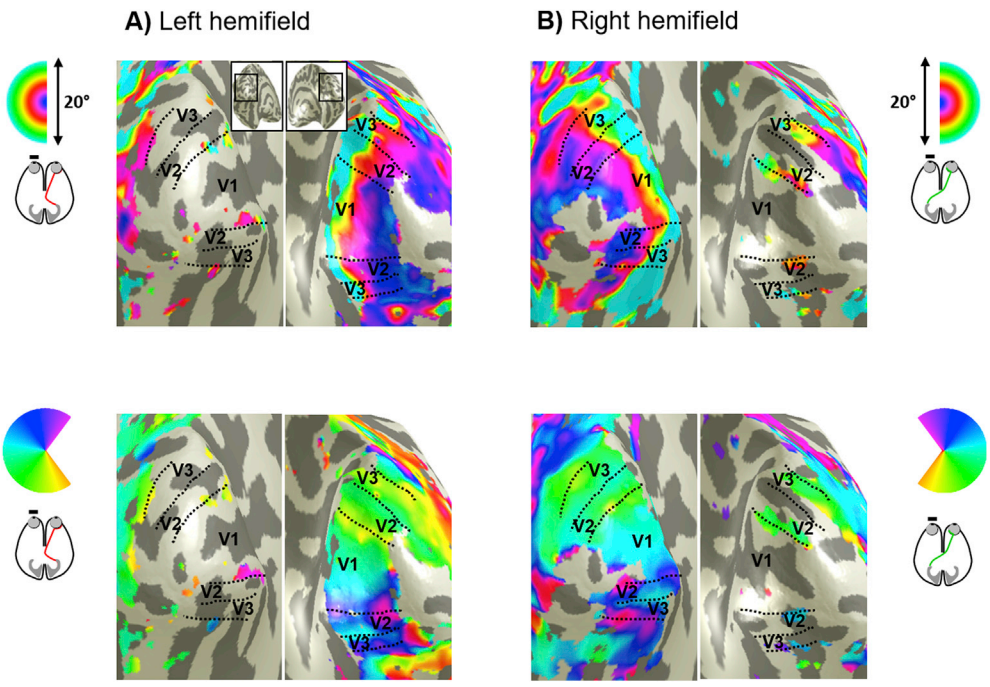

Fig. 4. Visual field representations for unilateral stimulation of the right eye in a control participant. Eccentricity (top row) and polar angle maps (bottom row) on the inflated occipital cortex for left **(A)** and right **(B)** hemifield stimulation. In both cases, orderly eccentricity and polar angle maps were obtained predominantly on the hemisphere contralateral to the stimulated hemifield. Residual ipsilateral representations of the vertical meridians and fovea were observed in V1–V3 as reported previously (Hoffmann et al., 2003; Tootell et al., 1998). Note that this residual representation is clearly different from the additional third hemifield map in CHP (Fig. 5C) which is more widespread and follows a retinotopic progression.

(ROI_{3maps}). For this purpose, we determined the goodness of fit of the pRF model, i.e. mean variance explained (VE; Fig. 7B). Although the area of cortex mapping the residual contralateral input of the right eye is smaller, the VE associated with this input does not appear to be markedly reduced compared to those driven by the normal and abnormal inputs of the left eye. These findings indicate the propagation of the triple hemifield input from V1 to the extrastriate cortex. The assessment of pRF-size properties and V1-referred connective field (CF) estimates in V2 and V3 suggest that the cortico-cortical connectivity underlying this propagation might be altered in CHP. This is depicted for the overlap of the three hemifield representations (ROI_{3maps}) in left V1–V3 in Figure S4 together with a detailed account on the respective pRF and CF signatures and their peculiarities in CHP.

Finally, the visual field coverage was assessed with pRF center and coverage plots as depicted in Figures S5 and S6, respectively. The pRF center distributions for the left and right V1 – V3 are presented for all four stimulation conditions for both CHP and a control participant (Figure S5). For the control, pRF centers predominantly cover the contralateral visual field; far less voxels represent the ipsilateral visual field, possibly due to a combination of the residual ipsilateral representation, noise intrusions and modelling limitation (see below). In CHP, the pRF centers of left V1 – V3 were predominantly located on the left and right hemifields following the left and right hemifield stimulation of the left eye, respectively (Figure S5 A, top panels).

For the left hemifield stimulation of the right eye, the pRF centers of the left V1 and V2 were mainly located in the upper left quadrant, whereas the pRF centers of the left V3 were mostly in the right hemifield (Figure S5 A, bottom left panel); as the right hemifield was actually not stimulated here, the latter is taken as an indication of the limitations of the model fit to the actual stimulus time course. Similarly, other ipsilateral extension into the non-stimulated hemifields, are partially due to the use of a circularly symmetric 2D Gaussian for the pRF model. Application of asymmetric models or models with minimal *priori* assumptions might reduce this ipsilateral coverage (Amano et al., 2009; Lee et al., 2013; Zeidman et al., 2018). Importantly, for the right eye's input during right hemifield stimulation, the pRF centers of these areas were primarily located in the right hemifield (Figure S5 A, bottom right panel), which reflects the residual normal input of the right eye to the left V1 (see also the corresponding pRF center values in control, Figure S5 C). This illustrates for the left visual areas in CHP, a combination of the pattern of representations typical of complete achiasma with the additional input from a third representation mediated by the right eye's input. In contrast, CHP's right visual areas are dominated by right eye input mediating representations from both visual hemifields (Figure S5 B, bottom panels), i.e., the typical hallmark of complete achiasma, with only little left eye input from the contralateral hemifield, found specifically a lower quadrant representation (Figure S5 B, top left panel).

The pRF-center findings are complemented by the visual field coverage plots which depict a combination of pRF center and size estimates (Amano et al., 2009). For clarity, only the coverage plots of V1 are presented in Figure S6. In principle, similar results are indicated by both pRF-center and visual field coverage plots. However, due to the incorporation of the pRF-sizes in the coverage plot, their coverage is more extensive than for the pRF center plots. In combination with the large pRF-size estimates for left V1 upon right hemifield stimulation of the right eye (compared to the corresponding pRF sizes for both left and right hemifield stimulation of the left eye, see Figure S4 A), this results in almost full field coverage for this condition. It should be highlighted that since the observed atypicalities in the left V1 do not occur for the coverage maps of the right V1, the inherent constraints of the pRF model should not be regarded as the only explanation. Other reasons, such as elevated noise in the data associated with imperfect fixation, may also lead to the observed ipsilateral extension of the visual field coverage maps.

4. Discussion

In the case of chiasma hypoplasia examined here, input from three visual hemifields converges onto the same cortical area. This puts a critical challenge on the organization of the visual cortex, which normally comprises a retinotopically aligned overlay of only two maps. The current study, therefore, provides novel insights into the scope and mechanisms of human visual system development and plasticity. Using high-resolution fMRI at 7T, DWI and fMRI-based pRF mapping at 3T, we report asymmetrical crossing of the nasal fibers of the two eyes that results in three overlaid representations of opposing hemifields on the left visual cortex. These findings suggest that the scope of cortical plasticity in the human visual system is sufficient to accommodate input from three

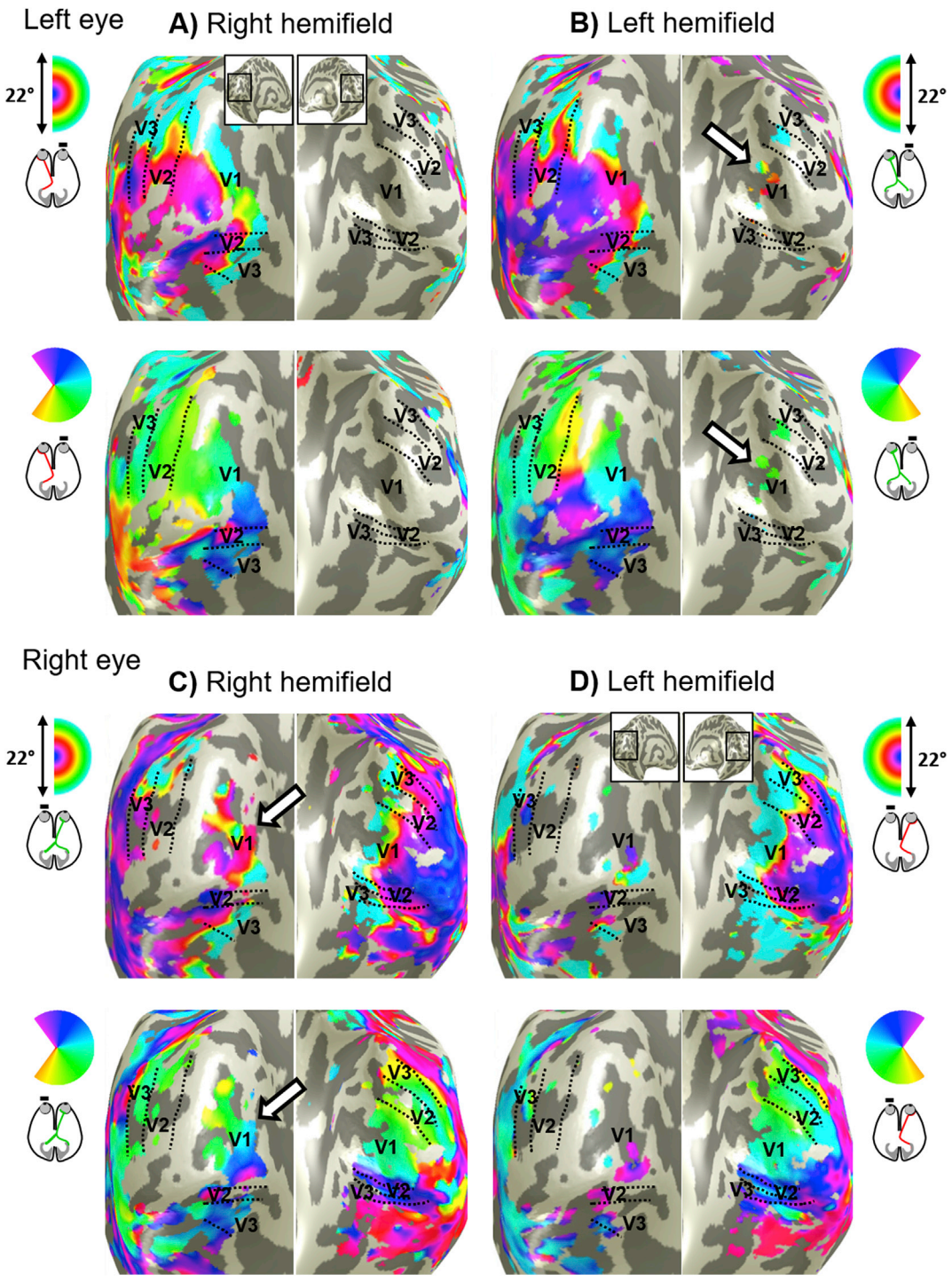

Fig. 5. Visual field representations for hemifield pRF-mapping in CHP for right and left eye stimulation. Eccentricity (top row in each panel) and polar angle (bottom row in each panel) maps are depicted on the inflated occipital cortex of CHP. For left eye stimulation, orderly eccentricity and polar angle maps are obtained on the left hemisphere for both right and left hemifield stimulation **(A, B)** and vice versa for right eye stimulation **(C, D)**. In addition, there is normal input to the hemisphere contralateral to the stimulated eye (white arrows). It is small for left eye stimulation and sizable for right eye stimulation, where it spans the entire polar angle range. The residual ipsilateral activation observed on the left hemisphere during left hemifield stimulation of the right eye **(D)** is reminiscent of the residual ipsilateral representation of the fovea and vertical meridian in controls (see Fig. 4). Furthermore, the considerable activation on the anterior regions of dorsal V3 observed for the aforementioned stimulation condition **(D)** is likely due to the callosal projections leading to binocular interactions at intermediate visual areas, as reported in complete achiasma (Davies-Thompson et al., 2013).

visual hemifields.

The retinotopically registered overlay of the representation of visual hemifields is a key property of the primary visual cortex. Remarkably, this is not only observed in the neuro-typical visual system, where these two maps comprise the binocular input of the contralateral visual hemifield it also holds for conditions with abnormal predominantly monocular input, as achiasma, albinism, or FHONDA (Ahmadi et al., 2019; Hoffmann et al., 2012, 2003). While the two maps segregate into ocular dominance domains in the neuro-typical case, they segregate into hemifield domains (Guillery et al., 1984; Olman et al., 2016) for

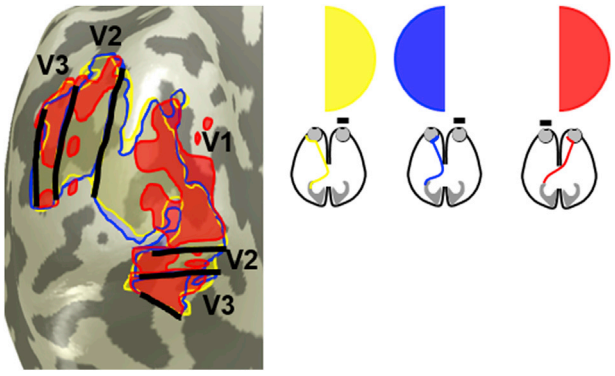

Fig. 6. Overlapping representation of the input from three hemifields in the left occipital lobe of CHP (based on the data shown in Fig. 5). The portions of visual cortex activated by stimulation of the left and right hemifield via the left eye [as typical for complete achiasma (Hoffmann et al., 2012)], colored yellow and blue, and of the right hemifield (as specific to the present case of CHP), colored red, are arranged as transparent overlays and combined into a single inflated representation of the occipital lobe.

conditions with congenital chiasma malformations. This is taken as evidence for largely unaltered geniculo-striate connections despite congenitally abnormal input to the LGN (Hoffmann and Dumoulin, 2015), as summarized in Fig. 8A and B. In fact, it appears that the neuro-typical geniculo-striate projection is in general largely unaffected by enhanced or absent crossing at the optic chiasm as in albinism/FHONDA or achiasma, respectively (Ahmadi et al., 2019; Hoffmann and Dumoulin, 2015). Consequently, we asked which cortical organization pattern would result from such stability in the geniculo-cortical projections in the present case of chiasma hypoplasia, in whom the left V1 receives triple hemifield input. Such an input is expected to result in a combination of the normal organization, i.e. ocular dominance domains (Fig. 8A), and the organization found in complete achiasma, i.e. hemifield domains (Fig. 8B) as depicted in Fig. 8C: the abnormal ipsilateral input from the left nasal hemiretina and the residual normal input from the right nasal hemiretina are expected to converge into the same domain (Fig. 8C). In the absence of geniculo-striate rewiring, the resulting cortical organization pattern is a retinotopic representation of the contralateral visual hemifield, via the left eye, that is interleaved with combined retinotopic representations of the ipsilateral and contralateral hemifield, via the left and right eye respectively. We, therefore, termed it in analogy to the nomenclature introduced previously (Hoffmann and Dumoulin, 2015), 'Interleaved Combined Representation'. In fact, such a pattern would result in the macroscopic cortical mapping we observed in the left occipital lobe. It should be noted though that the domain receiving input from the right visual hemifield, receives input from both eyes, thus reducing the differential activation via the two eyes. Further, we can, at present, not tell whether the neuronal populations representing the right hemifield input from both eyes segregate into distinct neuronal populations, due to the unavailability of data with sufficient resolution. Taken together, stable geniculo-striate projections still hold true even in the presence of triple input as observed in CHP. This conservative projection scheme, therefore, appears to be the most parsimonious concept to explain the cortical maps observed in a set of congenital projection abnormalities of the optic nerves, i.e. for enhanced, reduced or absent crossing.

Remarkably, the triple hemifield input to the left hemisphere affects only, albeit extensively, part of the primary visual cortex. In fact, another part of the visual cortex receives largely exclusive input from both hemiretinae of the left eye, as typical for complete achiasma. As a consequence, there is a coexistence of the 'Interleaved Representation' (Fig. 8B) and 'Interleaved Combined Representation' (Fig. 8C), occupying different regions of the left primary visual cortex. This is in accordance with the reports of animal models of albinism indicating a mixed organization pattern in the primary visual cortex (Cooper and Blasdel, 1980). Taken together, this suggests that the relevant adaptive developmental mechanisms can act locally.

Consistent with the reports on complete achiasma (Davies-Thompson et al., 2013; Hoffmann et al., 2012; Olman et al., 2016; Victor et al., 2000), the participant of the present study made effective use of vision in daily life, including sport activities and reading, and did not present specific visual field defects. Nevertheless quantitative testing is required to assess the behavioral consequences of chiasma hypoplasia and the intactness of the visual perception in CHP. Despite the binocular input to the left visual cortex, the disruption of binocular and stereo-vision is expected in CHP due to vertical and horizontal deviations between the two eyes. This suggests that there is no relevant interaction of the three representations in the left visual cortex.

In analogy to findings in other conditions with chiasma abnormalities (Klemen et al., 2012; Olman et al., 2016; Victor et al., 2000), the three

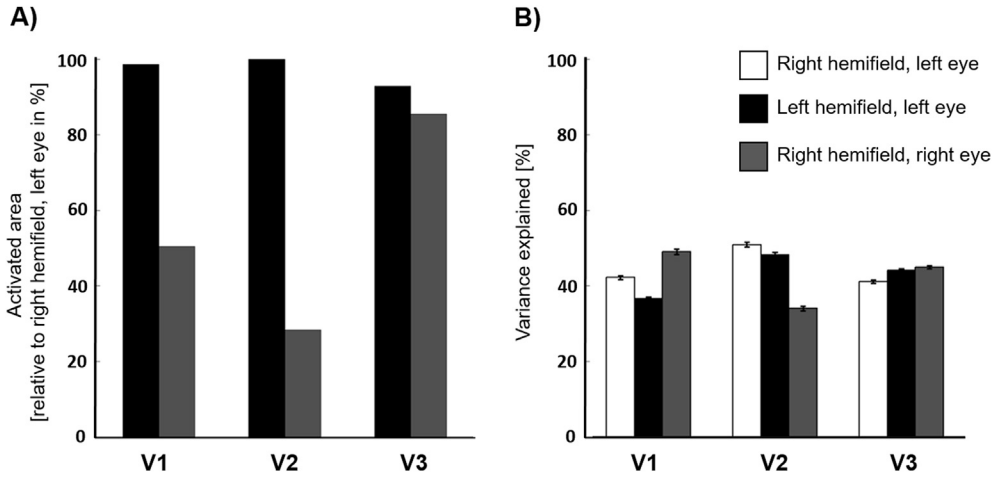

Fig. 7. Activated area and goodness of pRF model fit across left hemisphere V1–V3 of CHP. A) Activated area (normalized with respect to right hemifield, left eye stimulation condition) of left V1–V3 for left hemifield stimulation of the left eye (black bars) and right hemifield stimulation of the right eye (gray bars). For left hemifield stimulation of the left eye, the activated area of the left V1–V3 does not decrease below 92%. For the right hemifield stimulation of the right eye, the relative activated area of V1, V2 and, V3 is smaller, covering 50%, 28%, and 85%, respectively. **B)** Comparison of the goodness of fit, i.e. mean variance explained (VE) ± SEM, of the pRF model between right and left hemifield stimulation of the left eye (white and black bars) and right hemifield stimulation of the right eye (gray bars) in V1–V3 restricted to the overlapping area of the three maps (ROI_{3maps}). The VE for all three maps is relatively similar in V1 and V3 ranging from (49-37%) and (41–45%), respectively. For V2 it is reduced to 34% for the right hemifield right eye condition.

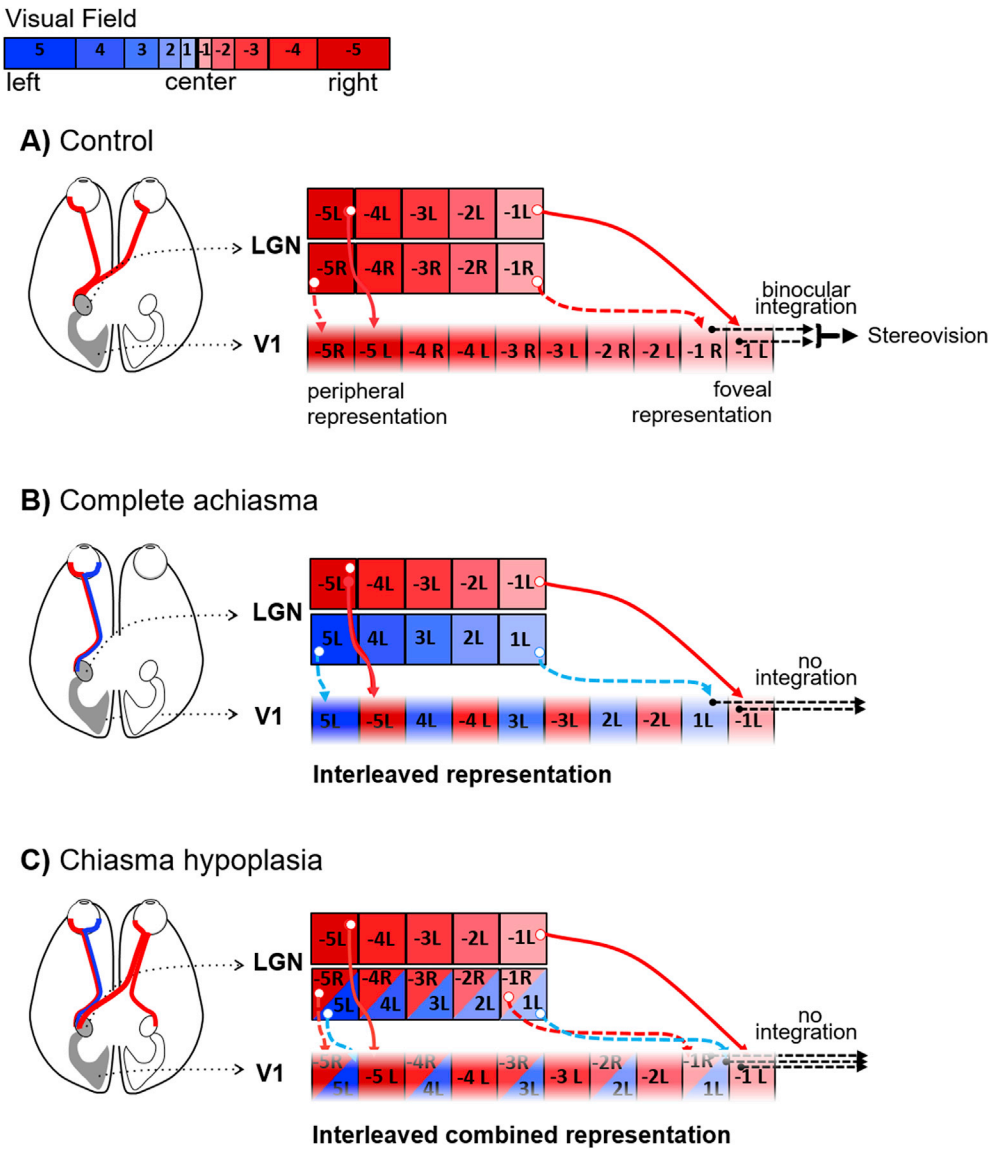

Fig. 8. Schematic of visual field representations in primary visual cortex for control, complete achiasma and chiasma hypoplasia. A) Control. The binocular input to the left LGN is organized as retinotopic maps of the right visual field (color coded red; negative numbers) that are separate for each eye (subscript indicates L – left, R – right eye input; the LGN is schematized as only two LGN layers with input from either eye). The geniculo-striate projections (solid red arrows for the left and dashed red arrows for the right eye input) result in interleaved retinotopic representations of the two eyes in V1. The integration of binocular input from corresponding locations in the contralateral visual field leads to binocular and stereovision. **B)** Complete achiasma. The left LGN receives monocular input from the nasal (blue) and from the temporal (red) hemiretina of the ipsilateral eye (i.e. left the eye, indicated by the subscript L). Consequently, there is in addition to the normal input from the contralateral visual field (red fields with negative numbers) input from the ipsilateral visual field (blue fields with positive numbers). This leads to an interleaved representation of opposing hemifields in V1, which is associated with a conservative, i.e. unchanged, geniculo-striate projection despite the abnormal LGN input (dashed cyan arrows). The absence of integration of the monocular input from opposing visual hemifields counteracts cross-talk of information between the hemifield. **C)** Chiasma hypoplasia. The left LGN receives binocular input from the contralateral visual field (red fields with negative numbers) as well as ipsilateral input (blue fields with positive numbers) only from the left eye. The triple hemifield input to the left LGN is organized as an interleaved representation of the contralateral visual field from the left eye (red fields with negative numbers in separate boxes) and combined representation of opposing hemifields from both eyes (red fields with negative numbers and blue fields with positive numbers in shared boxes). A conservative geniculo-striate projection to V1 would result in an interleaved combined representation pattern, obtained by the combination of cortical organization schemes for the control (A) and complete achiasma (B). Specifically, while the contralateral input of the left eye is incorporated via a separate domain, the contralateral input of the right eye together with the ipsilateral input of the left eye are assumed to be accommodated within a shared domain. Similar to complete achiasma, no integration is expected to occur across the three hemifield representations, supporting independent processing of the three maps.

representations of the hemifields in the left primary visual cortex might drive visual perception independently. Further research addressing the independence of the three different maps is motivated by the current findings. Lack of integration of information across the ocular dominance and/or across the hemifield dominance domains in CHP would require plasticity of the intracortical micro-circuitry to cope with the abnormal visual input and to support independent processing of the three superimposed hemifields (Fig. 8).

Akin to other visual pathway abnormalities, it is therefore assumed that the aberrant representation in CHP is made available for relatively normal visual perception through the interplay of subcortical stability and cortical plasticity. The cortical plasticity might not be confined to changes in the intra-cortical connectivity and, in addition, affect the cortico-cortical connectivity as suggested by changes in pRF and CF size

estimates (Figure S4). It, therefore, appears that the extra-input from the right eye impacts on the cortico-cortical connectivity of the early visual areas in CHP.

Studying visual system abnormalities is a unique approach for advancing our insights into the interplay of pathology and plasticity directly in humans and for gaining an understanding of the underlying developmental principles. A common limitation, however, is the rarity of relevant conditions and hence the limited availability of affected individuals. This also applies to the field of congenital malformations of the optic chiasm. While the well-known enhanced crossing of the optic nerves in albinism is already a rare condition [1.17:000 (Grønskov et al., 2007);], reduced crossing, i.e. achiasma, is much rarer [< 50 cases published worldwide (Hoffmann and Dumoulin, 2015),]. In fact, fMRI-data have been reported in the past two decades for only 6 different individuals (Bao et al., 2015; Davies-Thompson et al., 2013; Hoffmann et al., 2012; Nguyen et al., 2018; Victor et al., 2000). Thus, investigating a subtype of achiasma, i.e. with the specific hypoplasia of the optic chiasm reported in the present study, is an exceptional case. As such, we did not have the opportunity to obtain additional data for this condition, neither from the present nor from other individuals, despite the potentially informative value of e.g. additional high-resolution fMRI data. Another limitation of investigating visual system pathologies is related to fixation instabilities. Particularly, the dependence of the retinotopic data on the fixation stability may be questioned. However, previous studies (Baseler et al., 2002; Levin et al., 2010) have shown that nystagmus and fixation instability result in an enlargement of the pRF sizes without having a major effect on the eccentricity and polar angle maps. The high quality of the retinotopic maps, i.e., systematic response signatures typical of retinotopic maps, in CHP implies sufficiently stable fixation, though it could have been ideal to record the fixation performance in each eye separately.

Furthermore, while the present case is unique, it shares features, previously reported for achiasma, i.e. the retinotopic overlay of opposing visual hemifields (Hoffmann and Dumoulin, 2015). This is taken as an indication of the overall quality of the functional data obtained. Specifically, the data-set allowed reproducing previous results, i.e. orderly eccentricity and polar-angle maps from opposing visual hemifields via the ipsilateral (left) eye, and adding a further feature, i.e. the third input to the left visual cortex via the contralateral (right) eye. Stimulus-induced deviations from central fixation would be expected to be specific to the visual stimuli applied. Importantly, the activation in the cortical region comprising the additional third input was reproducible for different stimulation conditions applied via the right eye, i.e., for bilateral stimulation (Fig. 2B) and for right hemifield mapping (Fig. 5C).

Further, the amount of the overlap between the 3T and 7T data could not be quantified due to inherent differences in data acquisition one of which was the acquisition of 2 distinct anatomical volumes with different spatial resolutions. The visual area boundaries obtained by the pRF mapping could have been projected to the 7T data at the expense of downsampling the high resolution anatomy acquired at 7T. Nonetheless, careful visual inspection suggests a high degree of overlapping activity in cortical regions receiving the additional third input in both stimulation conditions. We conclude that fixation instabilities are a highly unlikely source of the observed cortical triple maps.

It might be argued that the comparison of the observed findings in CHP with strabismic amblyopes with a similar level of visual acuity and strabismus might be more informative than that with healthy controls. However, the effects of amblyopia on the organization of the visual cortex remain controversial. While some studies suggest a shift in ocular dominance of neural activity toward the fellow eye (Goodyear et al., 2002; Crawford and Harwerth, 2004), others have found no alteration or shrinkage of the ocular dominance domains (Horton and Hocking, 1996). Importantly, it has been demonstrated that despite the increased pRF sizes for the amblyopic eye, the retinotopic representations are preserved in strabismic amblyopia (Clavagnier et al., 2015). It is therefore concluded that the interpretation of the observed striking cortical organization in CHP does not hinge on the comparison group.

In addition, a few methodological considerations should be addressed. In the present study, partial Fourier acquisition (Feinberg et al., 1986) was employed in the high-resolution fMRI data. This approach is commonly used to accelerate the acquisition time or shorten the echo train length, albeit at the cost of image blurring (Feinberg et al., 2018). The blurring can be mitigated by use of partial Fourier imaging with a higher factor or with full Fourier acquisition. This results in a prolonged TE, whereas minimal acquisition time and consequently reduced motion artifacts had a higher priority in this experiment. It should also be noted, that the accuracy of the DWI analysis depends on the angle of crossing fibers (Tournier et al., 2008). This limitation is of particular relevance to this study, where the analyzed groups displayed various angles between crossing fibers. To address this issue, the DWI data were collected with the custom protocol designed to resolve crossing fibers [b-value of 1600 s/mm^2 selected according to reported range of 1500–2500 s/mm^2, optimal for resolving two-way crossing (Sotiropoulos et al., 2013); high angular resolution granted by 128 unique gradient directions (Tuch et al., 2002)] and analyzed with the methods ensuring the optimal discrimination between separate fiber populations, such as the Multi-Tissue constrained spherical deconvolution (Jeurissen et al., 2014).

5. Conclusion

Congenital visual pathway abnormalities are powerful models to further our understanding of the scope of developmental stability and plasticity in the human visual system, which may impact on novel therapeutic approaches. Here, we demonstrate that the gross topography of the geniculo-striate projections in CHP remains chiefly unaltered resulting in triple hemifield input to the visual cortex. This reflects an unaltered geniculo-cortical axonal guidance by chemoaffinity gradients (Cang et al., 2005; McLaughlin and O'Leary, 2005), even in the face of severely erroneous input to LGN. The additional input to the left visual cortex is assumed to be incorporated by sharing the same domain between the abnormal input of the left eye and normal input of the right eye. This underlines that intra-cortical plasticity provides sufficient scope to accommodate highly atypical visual input for comparatively normal visual processing.

Author contributions

K.A., A.F., A.D.G., S.O.D., A.B.M., and M.B.H: Conceptualization, K.A., A.F., R.J.P A.D.G., R.Y., O.S., J.K., F.P., and M.B.H: Methodology, K.A., A.F., and R.J.P: Formal Analysis, K.A., A.D.G., A.B.M., and M.B.H: Investigation, K.A., R.J.P: Writing – Original Draft, K.A., A.F., R.J.P., J.K., O.S., F.P., S.O.D., A.B.M., and M.B.H: Writing – Review and Editing, M.B.H: Supervision.

Declaration of competing interest

The authors declare no competing interests.

Acknowledgements

The authors thank the study participants for their patience and cooperation. This work was supported by European Union's Horizon 2020 research and innovation programme under the Marie Sklodowska-Curie grant agreement (No. 641805) to S.O.D, A.B.M and M.B.H, by the German Research Foundation (DFG; HO2002 10-3) to MBH. A.F. was supported by the Biotechnology and Biology research council (BBSRC, grant number: BB/S006605/1).

Appendix A. Supplementary data

Supplementary data to this article can be found online at https://doi.org/10.1016/j.neuroimage.2020.116822.

References

Ahmadi, K., Fracasso, A., van Dijk, J.A., Kruijt, C., van Genderen, M., Dumoulin, S.O., Hoffmann, M.B., 2019. Altered organization of the visual cortex in FHONDA syndrome. NeuroImage, Mapping diseased brains 190, 224–231. https://doi.org/10.1016/j.neuroimage.2018.02.053.

Amano, K., Wandell, B.A., Dumoulin, S.O., 2009. Visual field maps, population receptive field sizes, and visual field coverage in the human MT+ complex. J. Neurophysiol. 102 (5), 2704–2718.

Andersson, J.L., Skare, S., Ashburner, J., 2003. How to correct susceptibility distortions in spin-echo echo-planar images: application to diffusion tensor imaging. Neuroimage 20, 870–888.

Apkarian, P., Bour, L., Barth, P.G., 1994. A unique achiasmatic anomaly detected in non-albinos with misrouted retinal-fugal projections. Eur. J. Neurosci. 6, 501–507.

Apkarian, P., Reits, D., Spekreijse, H., Van Dorp, D., 1983. A decisive electrophysiological test for human albinism. Electroencephalogr. Clin. Neurophysiol. 55, 513–531.

Bao, P., Purington, C.J., Tjan, B.S., 2015. Using an achiasmic human visual system to quantify the relationship between the fMRI BOLD signal and neural response. eLife 4, e09600. https://doi.org/10.7554/eLife.09600.

Baseler, H.A., Brewer, A.A., Sharpe, L.T., Morland, A.B., Jägle, H., Wandell, B.A., 2002. Reorganization of human cortical maps caused by inherited photoreceptor abnormalities. Nat. Neurosci. 5 (4), 364.

Bazin, P.-L., Pham, D.L., 2007. Topology-preserving tissue classification of magnetic resonance brain images. IEEE Trans. Med. Imag. 26, 487–496.

Brainard, D.H., 1997. The psychophysics toolbox. Spat. Vis. 10, 433–436.

Cang, J., Kaneko, M., Yamada, J., Woods, G., Stryker, M.P., Feldheim, D.A., 2005. Ephrin-as guide the formation of functional maps in the visual cortex. Neuron 48, 577–589.

Caruyer, E., Lenglet, C., Sapiro, G., Deriche, R., 2013. Design of multishell sampling schemes with uniform coverage in diffusion MRI. Magn. Reson. Med. 69, 1534–1540.

Clavagnier, S., Dumoulin, S.O., Hess, R.F., 2015. Is the cortical deficit in amblyopia due to reduced cortical magnification, loss of neural resolution, or neural disorganization? J. Neurosci. 35, 14740–14755.

Cooper, M.L., Blasdel, G.G., 1980. Regional variation in the representation of the visual field in the visual cortex of the Siamese cat. J. Comp. Neurol. 193, 237–253.

Crawford, M.L., Harwerth, R.S., 2004. Ocular dominance column width and contrast sensitivity in monkeys reared with strabismus or anisometropia. Invest. Ophthalmol. Vis. Sci. 45 (9), 3036–3042.

Davies-Thompson, J., Scheel, M., Lanyon, L.J., Barton, J.J.S., 2013. Functional organisation of visual pathways in a patient with no optic chiasm. Neuropsychologia 51, 1260–1272. https://doi.org/10.1016/j.neuropsychologia.2013.03.014.

Dumoulin, S.O., Wandell, B.A., 2008. Population receptive field estimates in human visual cortex. Neuroimage 39, 647–660. https://doi.org/10.1016/j.neuroimage.2007.09.034.

Feinberg, D.A., Hale, J.D., Watts, J.C., Kaufman, L., Mark, A., 1986. Halving MR imaging time by conjugation: demonstration at 3.5 kG. Radiology 161 (2), 527–531.

Feinberg, D.A., Vu, A.T., Beckett, A., 2018. Pushing the limits of ultra-high resolution human brain imaging with SMS-EPI demonstrated for columnar level fMRI. Neuroimage 164, 155–163.

Fracasso, A., Koenraads, Y., Porro, G.L., Dumoulin, S.O., 2016. Bilateral population receptive fields in congenital hemihydranencephaly. Ophthalmic Physiol. Optic. 36, 324–334.

Fracasso, A., Luijten, P.R., Dumoulin, S.O., Petridou, N., 2018. Laminar imaging of positive and negative BOLD in human visual cortex at 7 T. Neuroimage 164, 100–111.

Friston, K.J., Fletcher, P., Josephs, O., Holmes, A., Rugg, M.D., Turner, R., 1998. Event-related fMRI: characterizing differential responses. Neuroimage 7, 30–40. https://doi.org/10.1006/nimg.1997.0306.

Goodyear, B.G., Nicolle, D.A., Menon, R.S., 2002. High resolution fMRI of ocular dominance columns within the visual cortex of human amblyopes. Strabismus 10 (2), 129–136.

Grønskov, K., Ek, J., Brondum-Nielsen, K., 2007. Oculocutaneous albinism. Orphanet J. Rare Dis. 2, 43.

Guillery, R.W., Hickey, T.L., Kaas, J.H., Felleman, D.J., Debruyn, E.J., Sparks, D.L., 1984. Abnormal central visual pathways in the brain of an albino green monkey (Cercopithecus aethiops). J. Comp. Neurol. 226, 165–183. https://doi.org/10.1002/cne.902260203.

Haak, K.V., Winawer, J., Harvey, B.M., Renken, R., Dumoulin, S.O., Wandell, B.A., Cornelissen, F.W., 2013. Connective field modeling. Neuroimage 66, 376–384.

Han, X., Pham, D.L., Tosun, D., Rettmann, M.E., Xu, C., Prince, J.L., 2004. CRUISE: cortical reconstruction using implicit surface evolution. Neuroimage 23, 997–1012.

Harvey, B.M., Dumoulin, S.O., 2011. The relationship between cortical magnification factor and population receptive field size in human visual cortex: constancies in cortical architecture. J. Neurosci. Off. J. Soc. Neurosci. 31, 13604–13612. https://doi.org/10.1523/JNEUROSCI.2572-11.2011.

Hoffmann, M.B., Dumoulin, S.O., 2015. Congenital visual pathway abnormalities: a window onto cortical stability and plasticity. Trends Neurosci. 38, 55–65. https://doi.org/10.1016/j.tins.2014.09.005.

Hoffmann, M.B., Kaule, F.R., Levin, N., Masuda, Y., Kumar, A., Gottlob, I., Horiguchi, H., Dougherty, R.F., Stadler, J., Wolynski, B., Speck, O., Kanowski, M., Liao, Y.J., Wandell, B.A., Dumoulin, S.O., 2012. Plasticity and stability of the visual system in human achiasma. Neuron 75, 393–401. https://doi.org/10.1016/j.neuron.2012.05.026.

Hoffmann, M.B., Seufert, P.S., Schmidtborn, L.C., 2007. Perceptual relevance of abnormal visual field representations: static visual field perimetry in human albinism. Br. J. Ophthalmol. 91, 509–513. https://doi.org/10.1136/bjo.2006.094854.

Hoffmann, M.B., Tolhurst, D.J., Moore, A.T., Morland, A.B., 2003. Organization of the visual cortex in human albinism. J. Neurosci. Off. J. Soc. Neurosci. 23, 8921–8930.

Horton, J.C., Hocking, D.R., 1996. Pattern of ocular dominance columns in human striate cortex in strabismic amblyopia. Vis. Neurosci. 13, 787–795.

Huberman, A.D., Feller, M.B., Chapman, B., 2008. Mechanisms underlying development of visual maps and receptive fields. Annu. Rev. Neurosci. 31, 479–509.

In, M.-H., Speck, O., 2012. Highly accelerated PSF-mapping for EPI distortion correction with improved fidelity. Magn. Reson. Mater. Phys. Biol. Med. 25, 183–192.

Jeurissen, B., Tournier, J.-D., Dhollander, T., Connelly, A., Sijbers, J., 2014. Multi-tissue constrained spherical deconvolution for improved analysis of multi-shell diffusion MRI data. Neuroimage 103, 411–426.

Kaule, F.R., Wolynski, B., Gottlob, I., Stadler, J., Speck, O., Kanowski, M., Meltendorf, S., Behrens-Baumann, W., Hoffmann, M.B., 2014. Impact of chiasma opticum malformations on the organization of the human ventral visual cortex. Hum. Brain Mapp. 35, 5093–5105. https://doi.org/10.1002/hbm.22534.

Klein, B.P., Fracasso, A., van Dijk, J.A., Paffen, C.L., Te Pas, S.F., Dumoulin, S.O., 2018. Cortical depth dependent population receptive field attraction by spatial attention in human V1. Neuroimage 176, 301–312.

Klemen, J., Hoffmann, M.B., Chambers, C.D., 2012. Cortical plasticity in the face of congenitally altered input into V1. Cortex J. Devoted Study Nerv. Syst. Behav. 48, 1362–1365. https://doi.org/10.1016/j.cortex.2012.03.012.

Lee, S., Papanikolaou, A., Logothetis, N.K., Smirnakis, S.M., Keliris, G.A., 2013. A new method for estimating population receptive field topography in visual cortex. Neuroimage 81, 144–157.

Levin, N., Dumoulin, S.O., Winawer, J., Dougherty, R.F., Wandell, B.A., 2010. Cortical maps and white matter tracts following long period of visual deprivation and retinal image restoration. Neuron 65 (1), 21–31.

McLaughlin, T., O'Leary, D.D., 2005. Molecular gradients and development of retinotopic maps. Annu. Rev. Neurosci. 28, 327–355.

Muckli, L., Naumer, M.J., Singer, W., 2009. Bilateral visual field maps in a patient with only one hemisphere. Proc. Natl. Acad. Sci. Unit. States Am. 106, 13034–13039. https://doi.org/10.1073/pnas.0809688106.

Nguyen, C.T., Goh, C., Desmond, P., Abel, L.A., Lim, C.H., Symons, R.A., Hardy, T.G., 2018. Congenital achiasma and see-saw nystagmus in VATER syndrome association with hydrocephalus. J. Clin. Neurosci. 51, 63–65.

Olman, C.A., Bao, P., Engel, S.A., Grant, A.N., Purington, C., Qiu, C., Schallmo, M.-P., Tjan, B.S., 2016. Hemifield columns co-opt ocular dominance column structure in human achiasma. Neuroimage.

Pelli, D.G., 1997. The VideoToolbox software for visual psychophysics: transforming numbers into movies. Spat. Vis. 10, 437–442.

Puzniak, R.J., Ahmadi, K., Kaufmann, J., Gouws, A., Morland, A.B., Pestilli, F., Hoffmann, M.B., 2019. Quantifying nerve decussation abnormalities in the optic chiasm. Neuroimage: Clin. https://doi.org/10.1016/j.nicl.2019.102055.

Saad, Z.S., Glen, D.R., Chen, G., Beauchamp, M.S., Desai, R., Cox, R.W., 2009. A new method for improving functional-to-structural MRI alignment using local Pearson correlation. Neuroimage 44, 839–848.

Sami, D.A., Saunders, D., Thompson, D.A., Russell-Eggitt, I.M., Nischal, K.K., Jeffery, G., Dattani, M., Clement, R.A., Liassis, A., Taylor, D.S., 2005. The achiasmia spectrum: congenitally reduced chiasmal decussation. Br. J. Ophthalmol. 89, 1311–1317.

Smith, R.E., Tournier, J.-D., Calamante, F., Connelly, A., 2012. Anatomically-constrained tractography: improved diffusion MRI streamlines tractography through effective use of anatomical information. Neuroimage 62, 1924–1938.

Sotiropoulos, S.N., Jbabdi, S., Xu, J., Andersson, J.L., Moeller, S., Auerbach, E.J., Glasser, M.F., Hernandez, M., Sapiro, G., Jenkinson, M., Feinberg, D.A., 2013. Advances in diffusion MRI acquisition and processing in the human connectome project. Neuroimage 80, 125–143.

Takemura, H., Caiafa, C.F., Wandell, B.A., Pestilli, F., 2016. Ensemble tractography. PLoS Comput. Biol. 12, e1004692.

Tootell, R.B., Mendola, J.D., Hadjikhani, N.K., Liu, A.K., Dale, A.M., 1998. The representation of the ipsilateral visual field in human cerebral cortex. Proc. Natl. Acad. Sci. Unit. States Am. 95, 818–824.

Tournier, J.-D., Calamante, F., Connelly, A., 2013. Determination of the appropriate b value and number of gradient directions for high-angular-resolution diffusion-weighted imaging. NMR Biomed. 26, 1775–1786.

Tournier, J.D., Calamante, F., Connelly, A., 2010. Improved probabilistic streamlines tractography by 2nd order integration over fibre orientation distributions. In: Proceedings of the International Society for Magnetic Resonance in Medicine, p. 1670.

Tournier, J.-D., Yeh, C.-H., Calamante, F., Cho, K.-H., Connelly, A., Lin, C.-P., 2008. Resolving crossing fibres using constrained spherical deconvolution: validation using diffusion-weighted imaging phantom data. Neuroimage 42, 617–625.

Tuch, D.S., Reese, T.G., Wiegell, M.R., Makris, N., Belliveau, J.W., Wedeen, V.J., 2002. High angular resolution diffusion imaging reveals intravoxel white matter fiber heterogeneity. Magn. Reson. Med. Off. J. Int. Soc. Magn. Reson. Med. 48, 577–582.

Van de Moortele, P.-F., Auerbach, E.J., Olman, C., Yacoub, E., Uğurbil, K., Moeller, S., 2009. T1 weighted brain images at 7 Tesla unbiased for Proton Density, T2* contrast

and RF coil receive B1 sensitivity with simultaneous vessel visualization. Neuroimage 46, 432–446.
Victor, J.D., Apkarian, P., Hirsch, J., Conte, M.M., Packard, M., Relkin, N.R., Kim, K.H., Shapley, R.M., 2000. Visual function and brain organization in non-decussating retinal-fugal fibre syndrome. Cereb. Cortex 10, 2–22. N. Y. N 1991.
von dem Hagen, E.A.H., Hoffmann, M.B., Morland, A.B., 2008. Identifying human albinism: a comparison of VEP and fMRI. Invest. Ophthalmol. Vis. Sci. 49, 238–249. https://doi.org/10.1167/iovs.07-0458.
Waehnert, M.D., Dinse, J., Weiss, M., Streicher, M.N., Waehnert, P., Geyer, S., Turner, R., Bazin, P.-L., 2014. Anatomically motivated modeling of cortical laminae. Neuroimage 93, 210–220.
Wandell, B.A., Chial, S., Backus, B.T., 2000. Visualization and measurement of the cortical surface. J. Cognit. Neurosci. 12, 739–752.
Wandell, B.A., Dumoulin, S.O., Brewer, A.A., 2007. Visual field maps in human cortex. Neuron 56, 366–383.
Weber, K.P., Landau, K., 2013. Teaching NeuroImages: mind the gap! Postfixational blindness due to traumatic rupture of the optic chiasm. Neurology 80, e197–e198.
Zeidman, P., Silson, E.H., Schwarzkopf, D.S., Baker, C.I., Penny, W., 2018. Bayesian population receptive field modelling. Neuroimage 180, 173–187.